

## REVIEW ARTICLE

# Magnetron sputtering of transparent conductive zinc oxide: relation between the sputtering parameters and the electronic properties

**Klaus Ellmer**

Hahn-Meitner-Institut Berlin, Department of Solar Energetics, Glienicker Strasse 100,  
14109 Berlin, Germany

E-mail: [ellmer@hmi.de](mailto:ellmer@hmi.de)

Received 6 October 1999

**Abstract.** Magnetron sputtering of transparent conductive oxides (zinc oxide, indium tin oxide, tin oxide) is a promising technique which allows the deposition of films at low temperatures with good optical and electronic properties. A special advantage is the scalability to large areas. The principles underlying magnetron sputtering are reviewed in this paper. The growth process during magnetron sputtering is characterized by the bombardment of the growing film with species from the sputtering target and from the plasma. In addition to sputtered atoms with energies in the eV range, ions from the plasma (mostly argon) and neutral atoms (also argon) reflected at the target hit the growing film. Depending on the energy of these species and on the ion-to-neutral ratio the properties of the films vary. High energies ( $\geq 100$  eV), which occur mainly at low sputtering pressures lead to damage of the growing film, connected with mechanical stress, small crystallites and bad electrical parameters. Ion assisted growth with low ion energies (below about 50 eV) is advantageous as is a high ion-to-neutral ratio. A compilation of resistivities of magnetron sputtered zinc oxide films yields a limiting resistivity of  $2 \times 10^{-4} \Omega \text{ cm}$  for polycrystalline films. Based on the correlation between plasma parameters and film properties new research fields are anticipated.

(Some figures in this article appear in colour in the electronic version; see [www.iop.org](http://www.iop.org))

## 1. Introduction

The planar magnetron sputtering source was invented at the beginning of the seventies [1, 2]. Only some years later magnetron sputtering was a well established commercial technique for the deposition of metals and optical films. However, for the deposition of semiconductors (transparent conductive oxides (TCO) belong to the class of wide band gap semiconductors) magnetron sputtering was used much later. This was caused by the stronger requirements which have to be fulfilled for the preparation of high-quality semiconducting thin films. The fundamental difference between magnetron sputtering as a plasma process and thermally excited thin-film preparation methods (evaporation, chemical deposition methods) is the much higher energy input into the growing film, that can be achieved by magnetron sputtering [1, 2]. In order to tailor the film properties one has to adjust the energy input into the substrate depending on the desired film properties.

Compared to other thin-film deposition methods such as evaporation, chemical vapour deposition (CVD) or spray

pyrolysis, magnetron sputtering is characterized by the following advantages:

- low substrate temperatures (down to room temperature)
- good adhesion of films on substrates
- high deposition rates (up to  $12 \mu\text{m min}^{-1}$ ) [3]
- very good thickness uniformity and high density of the films
- good controllability and long-term stability of the process
- alloys and compounds of materials with very different vapour pressures can be sputtered easily
- by reactive sputtering in rare/reactive gas mixtures many compounds can be deposited from elemental (metallic) targets
- relatively cheap deposition method
- scalability to large areas (up to  $3 \times 6 \text{ m}^2$ ) [4].

Although today magnetron sputtering is widely used in industrial coating for architectural glass (low emissivity coatings), integrated circuits (metal films), flat panel displays (TCO films) or hard coatings (titanium nitride) there is

still need for further research, especially in the field of the deposition of semiconducting thin films.

In the following sections the principles of magnetron sputtering are summarized (section 2). In section 3 special attention is given to the species (and their energies) which hit the substrate during film growth. Results for the deposition of transparent conductive zinc oxide are given in section 4. This review is restricted to the preparation and properties of polycrystalline TCO films, although epitaxial TCO layers have also been prepared [5, 6]. In the last section of this paper the conclusions and an outlook are given.

## 2. Principles of magnetron sputtering

It took nearly 40 years from the first report of the magnetron sputtering principle by Penning in 1936 [7] until the invention of the planar magnetron, which is the work-horse in magnetron sputtering deposition today. The basic feature of a magnetron discharge is the confinement of the plasma in front of the target (cathode) [8, 9]. This is achieved by the combination of electric and magnetic fields [8]. The magnetic field strength is adjusted in such a way (about 50 to 200 mT) that the electrons are significantly influenced by the magnetic field while the ions are not. The electrons perform cycloidal orbits in the crossed electric and magnetic fields, leading to a very high ionization efficiency. Therefore, magnetron discharges can be sustained at much lower pressures ( $<10^{-2}$  Pa) and/or higher current densities than the glow discharges without magnetic assistance.

A schematic diagram of a magnetron sputtering discharge is shown in figure 1(a). The magnetic field confines the electrons in front of the target in a torus-like plasma region which causes a non-uniform erosion of the target. The potential distribution in the discharge, i.e. between the target and the substrate, is essential for the sputtering and the deposition of the film. This potential distribution determines the energies of the ions and neutral species which contribute to the deposition process. The external discharge parameters such as working pressure, discharge power, design of the magnetic field (i.e. balanced or unbalanced magnetrons) and the excitation mode (dc or rf) influence the potential distribution and hence the particle energies. Most of the results reported in this review paper were obtained with balanced magnetrons. Many authors did not specify the type of magnetron used. For dc and rf excitation the potential distributions are shown schematically in figures 1(b) and (c).

Due to the different ionization mechanisms in dc and rf discharges the potential distributions are significantly different for these two excitation modes. The discharge voltage, i.e. the negative dc voltage which is measured at the target, is much lower for rf compared to dc excitation (figure 2(a)). This large difference (up to a factor of seven at low power) is caused by different processes at the target and in the plasma body which govern the dc and the rf magnetron discharge [10, 11]. The dc discharge is based upon the generation of ion-induced secondary electrons at the cathode (target). Therefore, large target voltages are necessary to sustain the plasma because the electron emission increases almost linearly with the ion velocity [12]. On the other hand, the rf plasma is mainly driven by ionization due to electrons

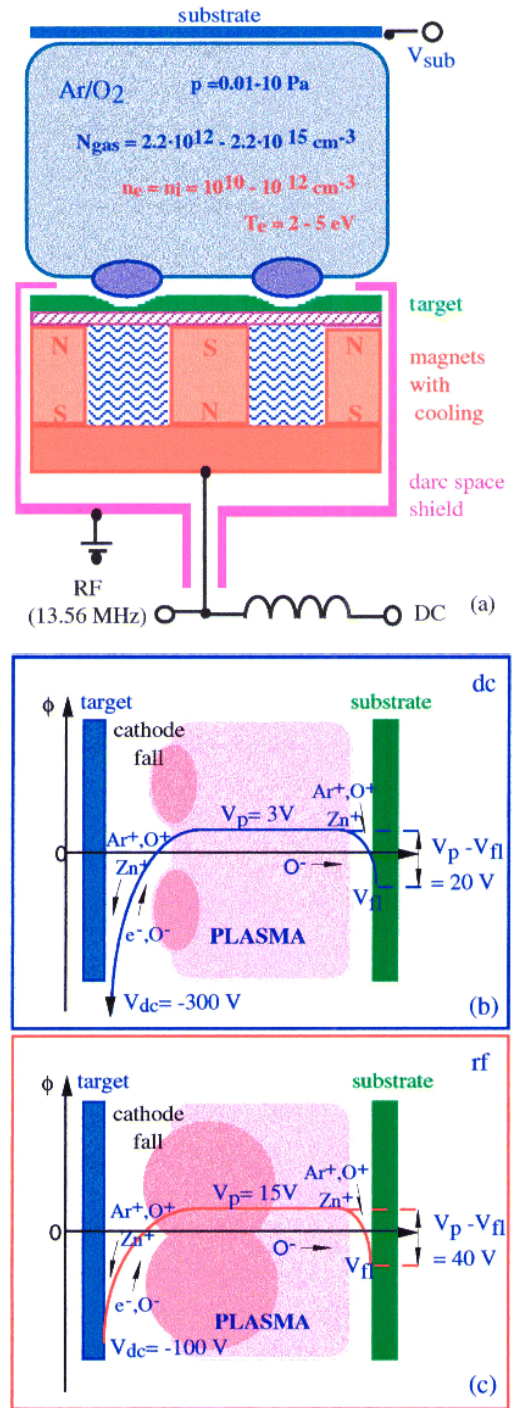


**Figure 1.** (a) Schematic diagram of a magnetron sputtering configuration for simultaneous rf and dc excitation. Typical plasma parameters ( $N_{gas}$ ,  $n_e$ ,  $T_e$ ) for a magnetron plasma are given. (b) Potential distribution in a dc excited magnetron sputtering discharge. (c) Potential distribution in a magnetron sputtering discharge, excited by rf.

which perform an oscillating motion in the plasma body. The electrons are able to follow the rf frequency of 13.56 MHz while the ions are not, due to their large inertia. This kind of excitation is much more effective compared to the ionization by non-oscillating secondary electrons and leads to lower target voltages in an rf discharge (figure 2(a)). However, the

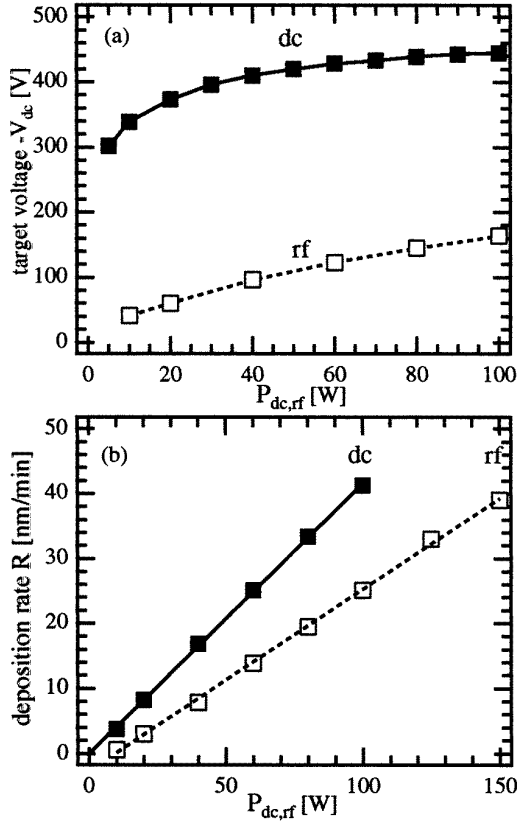


**Figure 2.** (a) Target voltages  $-V_{dc}$  and (b) deposition rate  $R$  dependent of the discharge power  $P_{dc,rf}$  for rf and dc excitation. The deposition parameters are ZnO target and  $p_{Ar} = 0.8$  Pa [16].

magnetic confinement of the electrons is, by far, not as good as in the dc discharge. This is caused by the fact that during the positive half-cycle the target acts not as cathode but as anode. Therefore, the plasma density in front of the substrate is significantly higher for rf compared to dc excitation.

The sputtering yield  $S$  depends linearly on the ion energy [13]:

$$S = \text{const}(E_{ion} - E_{thres}) = \text{const } e(V_p - V_{dc} - V_{thres}) \quad (1)$$

above a threshold energy  $E_{thres}$ . Yamamura and Itoh [14] gave a semi-empirical formula for the sputtering threshold energy:

$$E_{thres} = 8U_s(M_1/M_2)^{2/5} \quad (2)$$

where  $U_s$  is the surface potential barrier and  $M_{1,2}$  are the mass numbers of the ion and the target, respectively.

The low discharge voltages  $V_{dc}$  (rf) lead to significantly lower deposition rates for an rf magnetron discharge compared to a dc sputtering process under the condition of constant discharge power (figure 2(b)). The deposition rate is proportional to the discharge power, as expected [15]. This property of a magnetron sputtering discharge is advantageous for the controlling of a sputter deposition process. The dc process yields deposition rates that are a factor of 1.5–2 higher than that for rf sputtering.

For dc sputtering the deposition rate starts to increase from zero power. In the case of rf excitation a threshold power for sputtering of 10 W is observed (figure 2(b)), due to

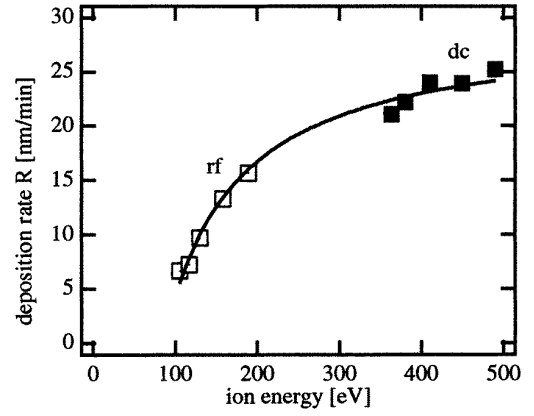


**Figure 3.** Deposition rate depending on the ion energy  $E_{ion} = e(V_{pl} - V_{dc})$ . This figure contains data from dc and rf sputtering. The full curve is a fit of a theoretical dependence (equation (4)) [17].

the low discharge voltages. When  $U_s$  is set to the sublimation energy of ZnO (7.6 eV) this threshold power corresponds to a threshold energy of about 85 eV, which is in good agreement with (2). The deposition rate  $R$  is proportional to  $S$ , the sputtering yield, and  $I(1 - \gamma)$ , with  $I$  the discharge current and  $\gamma$  the secondary electron emission coefficient:

$$R = \text{const } SI(1 - \gamma). \quad (3)$$

Combining (1) and (3) one obtains

$$\begin{aligned} R &= \text{const } eI(1 - \gamma)(V_{ion} - V_{thres}) \\ R &= \text{const } eI(1 - \gamma)|V_{dc}| \left( 1 + \frac{V_p - V_{thres}}{|V_{dc}|} \right) \\ R &= \text{const } eP(1 - \gamma) \left( 1 + \frac{V_p - V_{thres}}{|V_{dc}|} \right) \end{aligned} \quad (4)$$

where  $P$  represents the discharge power. Using (4), a universal curve for the deposition rate  $R$  as a function of the ion acceleration voltage ( $V_{pl} + |V_{dc}|$ ) can be fitted to the experimental data (figure 3). The following conclusions can be drawn from this graph:

- (i) the deposition rate is determined by the energy of the ions at the sputtering target.
- (ii) the energy of reflected argon atoms is higher for dc than for rf excitation.

The consequences of these conclusions will be discussed in section 3.

In the schematic potential distributions (figures 1(b) and (c)) it is shown that the positive ions ( $\text{Ar}^+$ ,  $\text{O}^+$ ,  $\text{Zn}^+$ ) are accelerated in the cathode fall  $V_p - V_{dc}$  towards the cathode, leading to the sputtering of the target. On the other hand, electrons and negative ions ( $\text{O}^-$ ) move from the target to the substrate. Together with reflected neutral argon atoms energetic negative ions can reach the substrate and will influence the layer growth. In the case of the rf discharge however, the plasma torus is more extended towards the substrate [11] as schematically shown in figure 1(c).

This is easily seen by visual inspection of a magnetron discharge excited by dc and rf. It causes a higher plasma

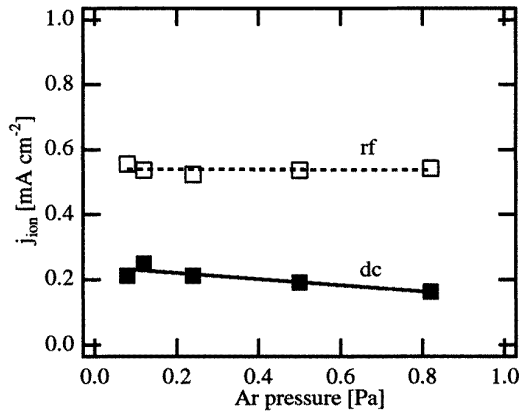


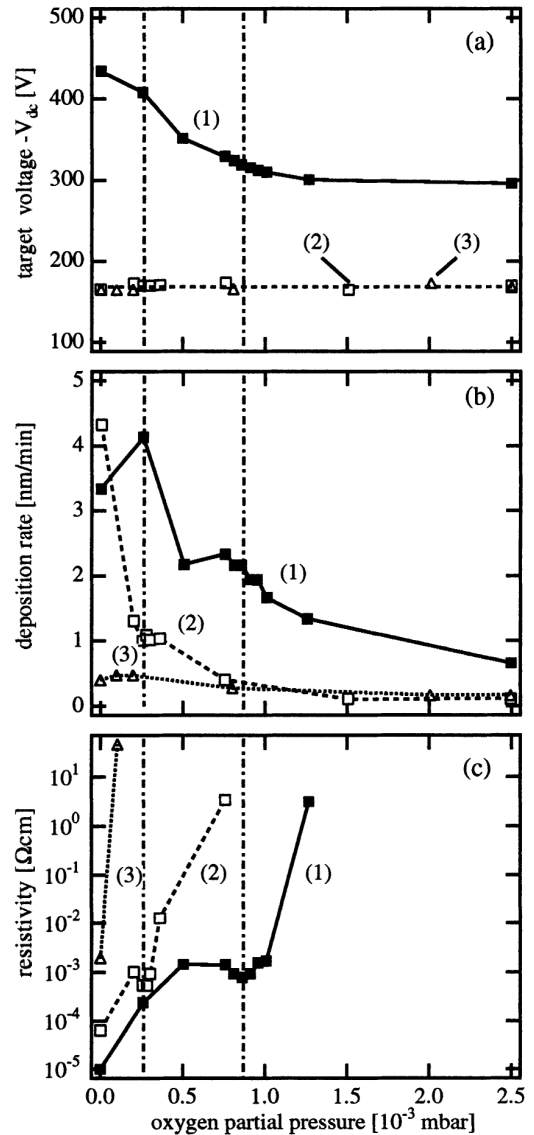
**Figure 4.** Ion saturation current density dependence on the working pressure for dc and rf excitation. The sputtering parameters are ZnO target and  $P = 50$  W [17].

density in front of the substrate for rf excitation and hence a higher ion saturation current to the growing film. In figure 4, the ion saturation currents on a floating substrate are shown depending on the working pressure for constant dc or rf power. It can be seen that the ion current on a substrate is nearly independent of the pressure below 1 Pa, which means that charge exchange collisions in the plasma sheath in front of the substrate do not play any role. The current density for rf excitation is about 2.5 times higher, pointing to the higher plasma density in front of the substrate.

The potential distribution in front of a floating substrate is such that the electrons are kept away from the substrate. Therefore, only electrons of sufficiently high energy are able to surmount the potential barrier at the substrate and the electron current is low in comparison to a glow discharge. Neutral species and energetic negative ions (for instance  $O^-$ ) of course are able to hit the substrate.

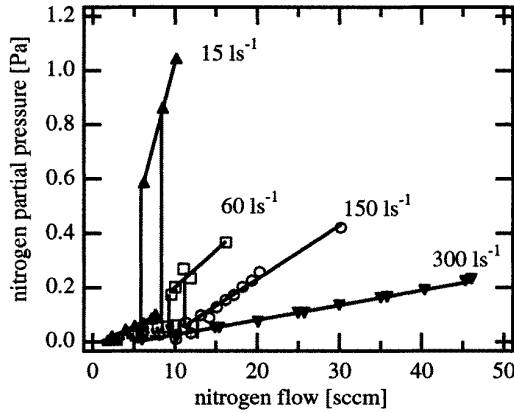
Up to now, only sputtering in pure argon has been considered, which requires a compound (oxidic) target for the preparation of an oxide. Although this method is simple it is not very well suited for commercial applications since ceramic targets are expensive and mechanically fragile. The other way for depositing a compound material (in our case oxides) is the so-called reactive sputtering, where a (cheap) elemental (mostly metallic) target is sputtered in an atmosphere of argon and a reactive gas (in our case oxygen). The reactive sputtering process is a very attractive method since in dependence on the reactive gas partial pressure layers with different chemical compositions and hence properties can be prepared. Furthermore, the deposition rates are generally higher compared to deposition from a compound target. Another advantage is the possibility of using dc power supplies. Ceramic compound targets are often too insulating to be sputtered by dc excitation. In this case rf power supplies have to be used, which are much more expensive than dc supplies. However, reactive sputtering often requires careful process control since the desired layer properties can only be obtained within a narrow parameter window.

Figure 5(a) displays the discharge voltage depending on the oxygen partial pressure for sputtering from different targets with dc and rf excitation. In the case of dc sputtering (curve 1) from a metallic target the discharge voltage exhibits



**Figure 5.** The dependence of the (a) discharge voltage  $-V_{dc}$ , the (b) deposition rate  $R$  and (c) the resistivity  $\rho$  on the oxygen partial pressure for three sputtering modes: (curve 1) dc from a metallic target Zn:Al 2 wt%, (curve 2) rf from a metallic target Zn:Al 2 wt% and (curve 3) rf from a ceramic target ZnO:Al<sub>2</sub>O<sub>3</sub> (2 wt%) [18]. The sputtering conditions are  $P = 100$  W,  $p_{Ar+O_2} = 0.5$  Pa and layer thickness  $\approx 0.5$   $\mu$ m. The vertical dot-dashed lines mark the positions of the resistivity minima.

a step-like behaviour at a specific oxygen partial pressure. Corresponding to this change of the target voltage, a decrease of the deposition rate can be seen (figure 5(b)). This observation can be explained by different surface states of the target depending on the oxygen partial pressure. At low pressures the target surface is metallic with a relatively low secondary electron emission and a high sputtering rate. With an increase in the oxygen portion in the sputtering atmosphere the target surface becomes oxidized; for zinc this is characterized by a higher secondary electron emission and a reduced sputtering rate. It is this transition from the metallic to the oxidized target mode that defines the process window in reactive (magnetron) sputtering. This can be seen for the case of ZnO:Al film preparation in



**Figure 6.** Nitrogen partial pressure dependence of the nitrogen flow during sputtering of silicon in Ar/N<sub>2</sub> for different pumping speeds, after Okamoto and Serikawa [19].

figure 5(c) where the resistivity is displayed as a function of the oxygen partial pressure. When the oxygen pressure is too low (metallic mode), the resistivity is low as is the optical transmission. Increasing  $p_{O_2}$  leads to the desired transparent ZnO:Al films with low resistivity. Even higher oxygen pressures improve the transparency of the films, but result in drastically higher resistivities due to the almost complete oxidation of zinc to ZnO and of aluminium to Al<sub>2</sub>O<sub>3</sub>. Doing the same by rf excitation, a similar picture for the behaviour of the deposition rate and the resistivity is obtained (curve 2). However, the discharge voltage does not show a step-like curve. This is caused by the fact that the rf discharge is nearly independent of the delivery of secondary electrons from the target.

For reactive sputtering a specific hysteresis and process stability behaviour of the oxygen partial pressure can occur when the oxygen flow is varied up and down during the sputtering. Some part of the reactive gas is consumed during the reactive sputtering process due to inclusion into the growing film. This gas consumption can be viewed as an internal pump for oxygen, reducing the oxygen partial pressure in the process chamber. When the pumping speed  $S_i$  of this internal pump (consisting of the target area and the total area deposited by the layer), given by

$$S_i = kTAR N_{film}/p \quad (5)$$

where  $T$  is the temperature,  $A$  is the coated area,  $R$  is the deposition rate,  $N_{film}$  is the molecular number density of the film ( $N_{ZnO} = 8.3 \times 10^{22} \text{ cm}^{-3}$ ) and  $p$  is the reactive gas pressure, becomes comparable to the external pumping speed  $S_e$  then hysteresis effects are observed. This has been shown very convincingly by Okamoto and Serikawa [19] for the sputtering of silicon in Ar/N<sub>2</sub> (see figure 6). By increasing the pumping speed from 15 to 300 l s<sup>-1</sup> the hysteresis of the nitrogen partial pressure as a function of the nitrogen flow vanishes. For stable operation of a reactive sputtering process a sufficiently high pumping speed is advantageous ( $S_e/S_i > 10$ ).

Sputtering at the change (turn over) between the metallic and the oxidic sputtering mode is selected for industrial coating processes since this yields the highest deposition

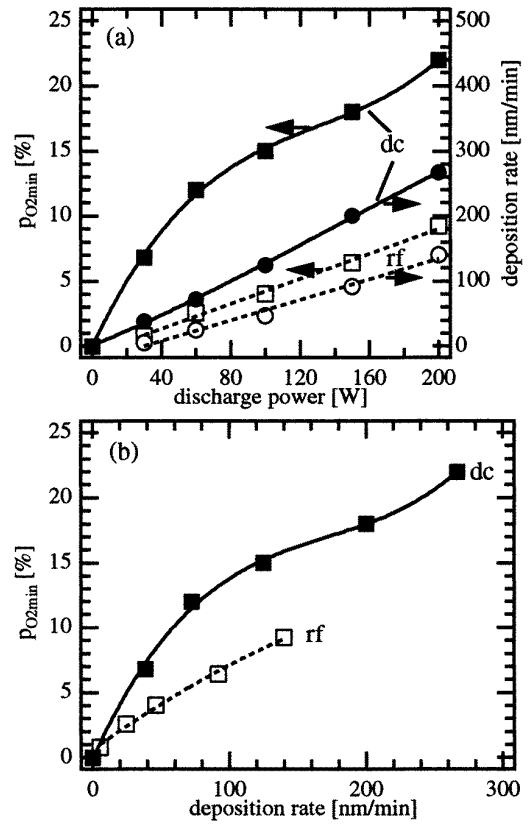


**Figure 7.** (a) Oxygen partial pressure  $p_{O_{2min}}$  (in per cent) where the resistance minimum occurs and deposition rate depending on the discharge power (dc and rf). (b)  $p_{O_{2min}}$  as a function of the deposition rate. The sputtering parameters are metallic target ZnAl 2 wt%, working pressure 0.5 Pa.

rates. For the deposition of TCO films close to this change between the metallic and oxidic target modes, a resistivity minimum is found (see figure 5(c)). Often a feedback control is used to stabilize the partial pressure of the reactive gas at the transition from the metallic to the oxidic target mode. For the feedback different physical principles are used:

- mass spectrometry [20, 21],
- optical emission spectroscopy [22, 23],
- oxygen sensor (Lambda probe, Leybold) [24],
- control of the discharge voltage [25, 26].

This turn over oxygen partial pressure  $p_{O_{2min}}$  depends on the deposition rate, that means on the discharge power as can be seen in figures 7(a) and (b). For dc reactive sputtering higher oxygen partial pressures are necessary compared to rf sputtering which is due to the higher fraction of 'reactive' (atomic and excited) oxygen in an rf discharge (see figure 13).

When the total pressure is increased the oxygen partial pressure  $p_{O_{2min}}$  that is necessary to deposit layers in the resistivity minimum increases, although the deposition rate remains constant, figure 8, and the lowest resistivities were always about  $3.5 \times 10^{-4} \Omega \text{ cm}$  [27]. This effect was also reported by Harding *et al* [28] for ZnO and Song *et al* for ITO [29].

A plausible explanation of this unexpected effect is related to the well known structure zone model of Thornton [30]. According to Thornton a high argon pressure during

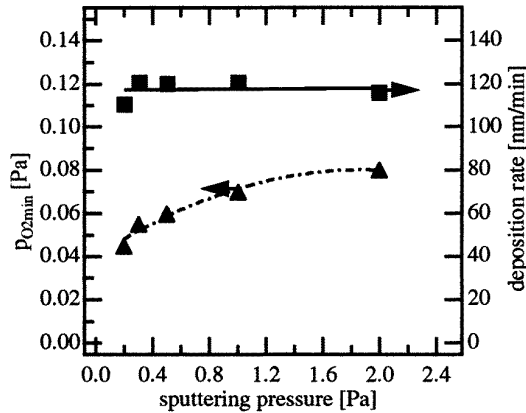


**Figure 8.** The deposition rate and oxygen partial pressure for the resistance minimum  $p_{O_{2min}}$  as a function of the sputtering pressure [27]. The sputtering parameters are metallic target ZnAl 2 wt%,  $P_{dc} = 100$  W.

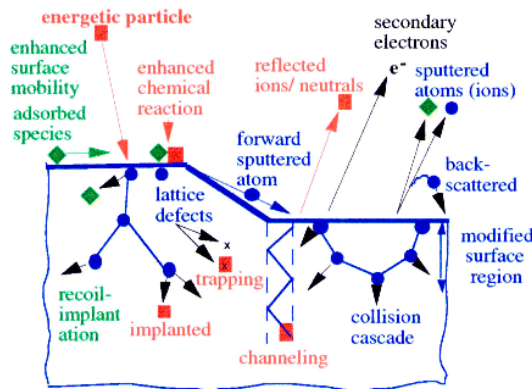


**Figure 9.** The effects of energetic particles on a solid surface during ion assisted growth (after Mattox [31]).

sputtering leads to layers with ‘tapered crystals separated by open, voided boundaries’ caused by the low energy of the sputtered species that contribute to the film growth. It is also the energy of the sputtered species that governs the oxidation efficiency at the surface of a growing film. At low pressures (0.2 Pa) the sputtered species (Zn, Al, O) possess a mean free path (4 cm) that is comparable to the target-to-substrate distance.

As a result of their high energy, these arriving particles have high surface mobility and therefore a higher chance to form ZnO with adsorbed oxygen atoms. At higher pressures the mean free path decreases (4 mm at 2 Pa) and the sputtered species undergo many collisions leading to a thermalization of the film-forming particles. Therefore, the surface mobility of these species decreases and hence the chance for oxidation also decreases. This is compensated by a higher oxygen partial pressure to achieve the resistivity minimum.

### 3. Species on a substrate during film growth

In addition to the sputtered species, ions and electrons are bombarding the substrate, as shown schematically in figure 1. Furthermore, the radiation from the plasma (and sometimes from the hot target surface) has to be taken into account. Mattox [31] summarized the effects of energetic particles on

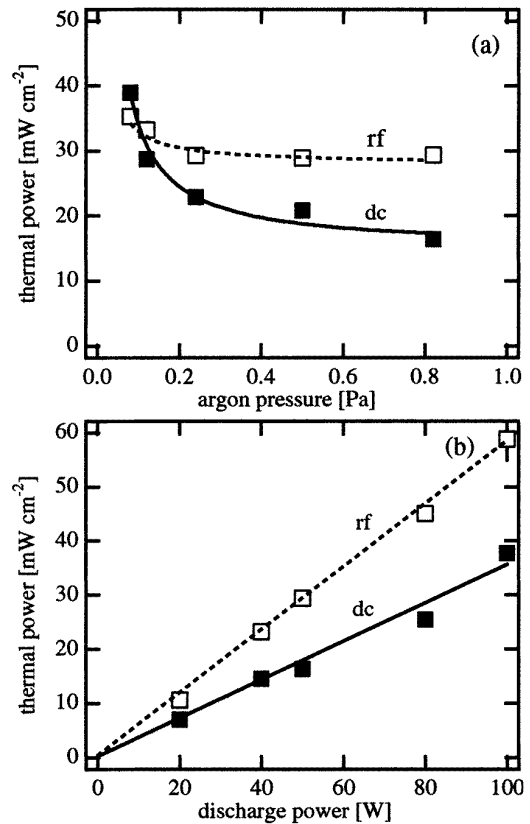


**Figure 10.** Thermal power at a floating substrate in dependence of the working pressure for dc (a) and rf (b) excitation [17]. The sputtering parameter is  $P = 50$  W.

a solid surface in the scheme shown in figure 9. From this figure it is clear that the energy of the particles is a further important quantity to characterize the growth process.

Although many authors report the dependence of film properties on external parameters such as working pressure, discharge power and substrate temperature, direct correlations between plasma parameters such as ion energy, electron temperature, ion-to-neutral ratio at the substrate and film parameters are very scarce in the literature for TCO-layers.

Concerning magnetron sputtering of zinc oxide such investigations have recently been undertaken by our group [16, 17]. To characterize the plasma and the energy flux to the substrate the following methods have been used [17]:

- calorimetry (total energy flux),
- Langmuir probe measurements (electron temperature, plasma density),
- plasma monitor measurements (mass and energy distributions of species hitting the substrate).

One of the results, the ion saturation current density against sputtering pressure, has already been presented in figure 4. The other important quantity is the total thermal power on the substrate, which is depicted in figure 10(a) as depending on the working pressure. The thermal power or the energy input determines the equilibrium temperature of the substrate and the growing film, which is reached after about 10 min. While the thermal power for rf excitation is nearly independent on the working pressure, the dc discharge shows



**Table 1.** Thermal power at the substrate for dc and rf sputtering (ZnO target,  $P = 50$  W,  $p_{Ar} = 0.8$  Pa,  $A$  is the area).

Energy source	$P/A$ (mW cm <sup>-2</sup> ) dc	$P/A$ (mW cm <sup>-2</sup> ) rf
$P_i$ (Ar <sup>+</sup> )	5.3	23.2
$P_e$ (e <sup>-</sup> )	1.9	5.5
$P_n^f$ (Zn, O)	2.3	0.7
sum	9.5	29.4
$P_{total}$	15.6	32.0
$P_{total} - \text{sum}$	6.1	2.6

a significant decrease of the thermal substrate power when varying the pressure from 0.08 to 0.8 Pa. The reason for this different behaviour will be explained below. In most cases the thermal load of the substrates is higher for rf compared to dc sputtering (at constant power).

Figure 10(b) shows the thermal power depending on the discharge power (dc and rf). As expected the thermal power is proportional to the discharge power. For both excitation modes, the curves start at zero discharge power. In the case of rf excitation this is in contrast to the deposition rate, which starts only at a power of about 10 W (see figure 2(b)). This means, the thermal load for rf sputtering is mainly determined by species originating not from the target, but from the plasma.

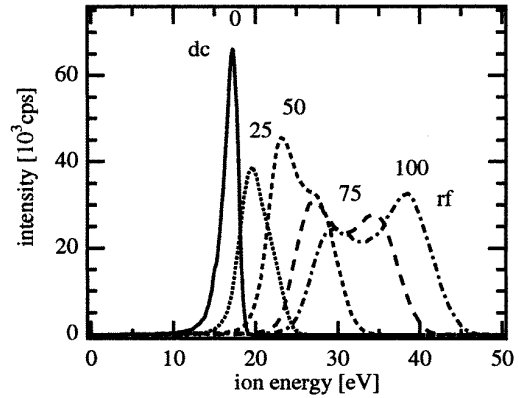
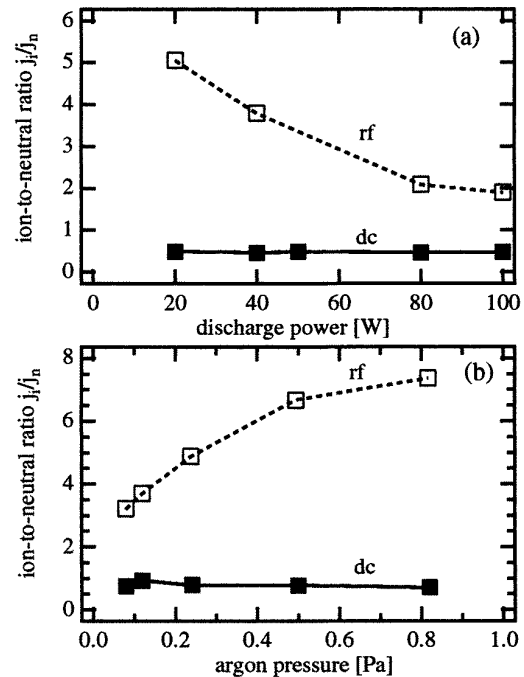
The energy input into the substrate (and the growing film) stems from different species [32]:

- electrons and ions from the plasma ( $P_e$  and  $P_i$ )
- neutral particles, which contribute to the film growth ( $P_n^f$ )
- (fast) neutral particles of the sputtering gas(es) ( $P_n$ )

From a detailed analysis for rf and dc sputtering from a ceramic ZnO target, the contributions of each source shown in table 1 were obtained [17].

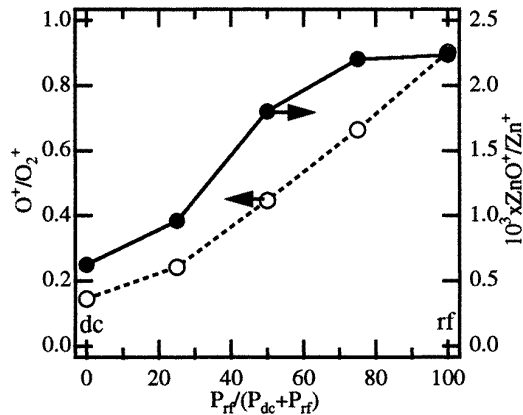
From this table it is obvious that the ion-induced energy input during rf sputtering is much higher (by about a factor of five) compared to dc sputtering. On the other hand, the difference between the measured total energy input ( $P_{total} - \text{sum}$ ) and the contributions from ions, electrons and film particles is higher for dc compared to rf excitation. This difference has to be attributed to energetic particles from the target—mainly reflected and neutralized argon ions [9]. This particle source was made responsible by Tominaga *et al* [33] for lateral variations of the resistivity during ZnO deposition. Due to the higher cathode fall in the dc discharge this part of the total energy input into the substrate is higher compared to the rf discharge. The energetic particles from the target have to travel the target-to-substrate distance (about 5 cm), where they suffer collisions with the sputtering gas atoms, leading to their thermalization. Therefore, the total energy input into the substrate for the dc discharge exhibits a significant pressure dependence (figure 10(a)).

On the other hand, the ion saturation current does not show a pressure dependence since the distance, these ions have to cross (the plasma sheath in front of the substrate) is much smaller and thus collision free in the pressure range below about 5 Pa. Aside from the higher ion saturation current density, the rf discharge is also characterized by


**Figure 11.** Energy distributions of  $^{36}\text{Ar}^+$  ions on a substrate at floating potential in dependence of the  $P_{dc}/(P_{dc} + P_{rf})$  ratio, given in numbers (in per cent) at different peaks [16].

**Figure 12.** Ion-to-neutral ratio  $j_i/j_n$  versus the (a) discharge power (dc and rf) and (b) the argon pressure [16].

higher ion energies at a floating substrate. This was shown by plasma monitor measurements for combined dc and rf excitation of a magnetron discharge (figure 11). The simultaneous excitation of a magnetron source allows the continuous tuning of the ion energy from low (dc) to high (rf) values. The dc ion energy distribution shows a sharp narrow peak, while the rf distribution exhibits a saddle-like broad shape, which is due to the modulation of the width of the plasma sheath by the rf.

An important parameter that governs the growth in ion-assisted deposition is the ratio of ions-to-neutrals  $j_i/j_n$  of the species impinging on a substrate. It was shown, both experimentally [34] and theoretically [35], that a high ion-to-neutral ratio is advantageous for (epitaxial) layer growth at low temperatures. For our experiments  $j_i/j_n$  was extracted from the ion saturation currents and from the deposition rates. Figure 12 shows the ion-to-neutral ratio against the



**Figure 13.** The ratio of atomic to molecular species  $O^+/O_2^+$  and  $Zn^+/ZnO^+$  depending on the  $P_{dc}/(P_{dc} + P_{rf})$  ratio [16].

discharge power and the argon pressure. The rf discharge is characterized by a much higher  $j_i/j_n$  ratio (a factor of four to ten) compared to the dc discharge. By also taking into account the higher ion energies in the rf case, the energy input due to argon ions is even higher compared to dc excitation. This very striking difference between rf and dc magnetron sputtering will be considered in more detail in section 4, when discussing the electrical properties.

A last result, which was derived from the plasma monitor measurements, is also worth a mention. The ratio of atomic to molecular ionized species ( $O^+/O_2^+$  and  $Zn^+/ZnO^+$ ) at the substrate is much higher for rf excitation compared to dc sputtering (figure 13). This points to the higher electron temperature and plasma density in an rf discharge, leading to a higher chance of dissociation of molecular species. The lower dissociation energy of ZnO (2.9 eV) in comparison to  $O_2$  (5.1 eV) is responsible for the much higher ratio  $Zn^+/ZnO^+$  compared to  $O^+/O_2^+$ . Due to ionization, dissociation and excitation of oxygen in the plasma, reactive species such as atomic and excited oxygen are formed. These species are favourable for the oxidation of metallic atoms in the growing film. Therefore, in an rf discharge smaller amounts of oxygen gas ( $O_2$ ) have to be added to get the desired transparent (oxidized) films (see figure 5(c)).

#### 4. Zinc oxide properties

The transparent conductive oxides belong to the class of wide band gap semiconductors (see table 2). The transparency in the visible wavelength region is due to their large band gap  $E_g \gtrsim 3$  eV. As typical representatives of compound semiconductors these oxides can be made conductive by intrinsic (defects) or extrinsic (dopants) charge carriers. Some of the properties of zinc oxide are collected in table 2 together with the properties of the other important TCO materials:  $In_2O_3$  and  $SnO_2$ . If these semiconductors are prepared intrinsically, i.e. without intrinsic or extrinsic dopants their resistivity is very high (of the order of  $\gtrsim 10^7 \Omega \text{ cm}$ ). The low resistivity which is required for their application as transparent electrodes can be achieved in two ways.

- Creation of intrinsic dopants by lattice defects (for instance oxygen vacancies or metal atoms on substitutional lattice sites) or

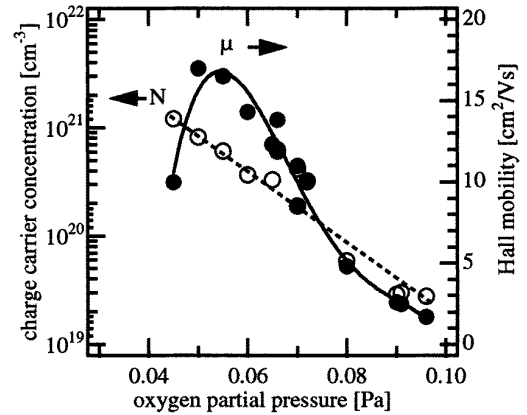


**Figure 14.** Charge carrier concentration and mobility of reactively sputtered ZnO:Al films depending on the oxygen partial pressure. The sputtering parameters are:  $p_{total} = 0.5$  Pa,  $P_{dc} = 100$  W, layer thickness  $d = 0.5 \mu\text{m}$ , deposition rate  $R = 115 \text{ nm min}^{-1}$  and target ZnAl 2 wt% [27].

- Introduction of extrinsic dopants (either metals with one additional conduction electron on zinc lattice sites or halogens with one additional electron on oxygen lattice sites).

The first possibility can be achieved during the deposition by carefully adjusting the oxygen partial pressure and the deposition rate. The other way is a reduction process of the oxide after deposition, for instance by annealing under vacuum or in a hydrogen-containing atmosphere [36]. However, it has been found that such films exhibit properties, which are not well suited for applications. First, the resistivity is only about  $10^{-2}$ – $10^{-3} \Omega \text{ cm}$ . Furthermore, these films are not stable under ambient conditions (especially at higher temperatures) due to the re-oxidation of the oxygen-deficient films. Therefore, in most cases extrinsic dopants are used for the preparation (table 2). In reality, during the preparation of doped oxide films by non-reactive and reactive sputtering both doping mechanisms occur simultaneously. By increasing the oxygen partial pressure during (or after) preparation the dopants on a metal lattice site become oxidized and hence lose its doping effect (see section 4.1). Another complication arises due to the variation of phases, structure and morphology when changing the deposition parameters, especially the oxygen partial pressure (see section 4.2).

##### 4.1. Electrical properties

When reactive sputtering from a metallic target is used, the resistivity exhibits a characteristic minimum depending on the oxygen partial pressure (see figure 5(c)). By Hall and resistivity measurements it was found for Al-doped ZnO films that this minimum originates from the oxygen pressure dependence of the mobility as shown in figure 14 [27]. Similar dependencies were found by others for ZnO,  $SnO_2$  and ITO [37–39]. The charge carrier concentration decreases by nearly two orders of magnitude when increasing the oxygen partial pressure from 0.04 to 0.1 Pa (corresponding to 8–20% of the total working pressure).



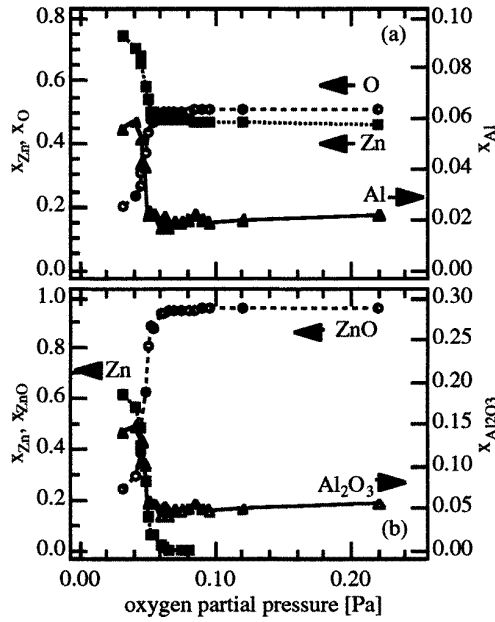


**Figure 15.** (a) Atomic composition of ZnO:Al layers and (b) phase composition calculated from (a) versus the oxygen partial pressure. The sputtering parameters are  $p_{total} = 0.5$  Pa,  $P_{dc} = 50$  W and  $d \approx 100$  nm [27].

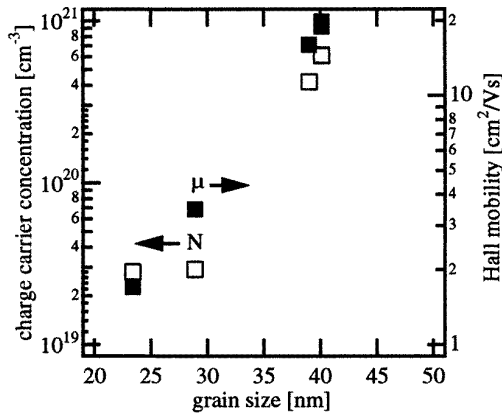


**Figure 16.** Charge carrier concentration and Hall mobility depending on the grain size (derived from the XRD spectra) of ZnO:Al films [27].

The highest carrier concentration of about  $1.5 \times 10^{21} \text{ cm}^{-3}$  corresponds to an electrical activation of about 60% of the aluminium dopants. Obviously, only part of the aluminium in the films is located on zinc lattice sites, where it can act as a dopant. With increasing oxygen partial pressure the charge carrier concentration decreases, which seems to be due to an oxidation of the aluminium in the film to alumina ( $\text{Al}_2\text{O}_3$ ); in the oxidized form the aluminium no longer acts as a dopant. This was concluded from the analysis by Rutherford backscattering (RBS) of the ZnO:Al films depending on the oxygen partial pressure (figure 15(a)).

At oxygen pressures below about 0.06 Pa the films exhibit a significant oxygen deficit leading to opaque films. The aluminium content of the films is about 2 at% (corresponding to the 2 wt% Al in the target) in the  $p_{O_2}$  region, where the films are transparent. For low oxygen partial pressures, a preferential build-in of Al into the layers

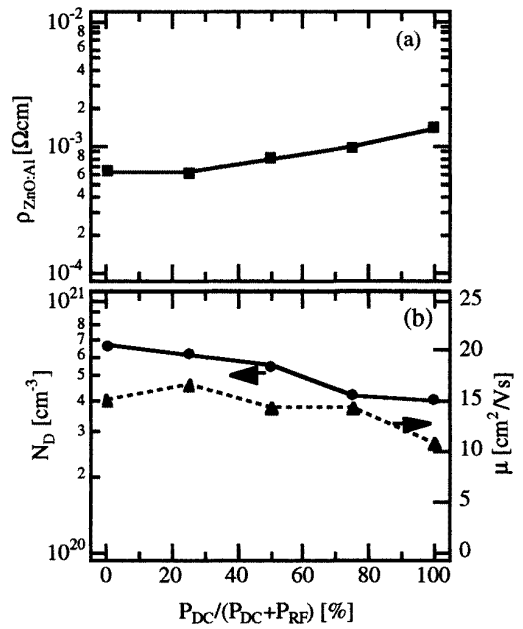


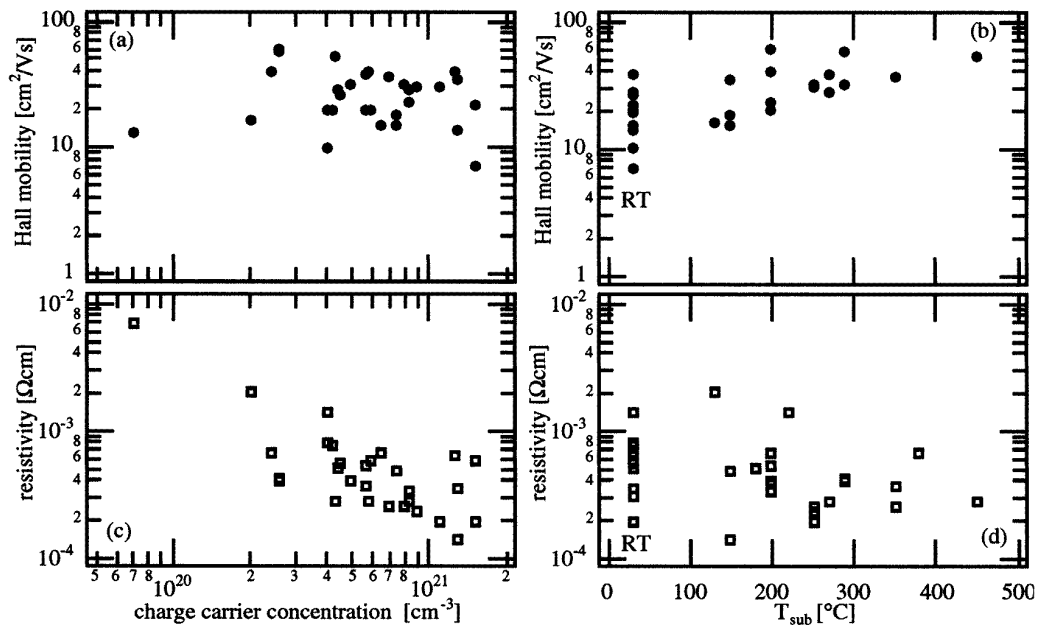
**Figure 17.** (a) Resistivity and (b) charge carrier concentration and Hall mobility of ZnO:Al films versus  $P_{dc}/(P_{dc} + P_{rf})$  for the simultaneous excitation by dc and rf [16].

is observed. The Al content increases by a factor of three. This can be explained by the stronger affinity of oxygen to Al and the higher probability of re-evaporation of zinc compared to aluminium, due to the low melting point of zinc [40]. From the composition shown in figure 15(a), the phase composition of the grown films was calculated with the assumption that only three phases occur: ZnO,  $\text{Al}_2\text{O}_3$  and metallic Zn (see figure 15(b)). The occurrence of the pure aluminium phase at low oxygen pressures was not taken into consideration since ZnO and  $\text{Al}_2\text{O}_3$  have very different heats of formation (3.6 eV for ZnO and 8.5 eV for  $\text{Al}_2\text{O}_3$ ), favouring the formation of alumina. The decrease of the oxygen pressure leads to a strong decrease of the ZnO phase and a corresponding increase of the unoxidized, i.e. metallic, zinc. It is this metallic zinc that leads to the darkening of the films at low oxygen partial pressures. However, regarding these anticipated phases, only the hexagonal zincite phase can be detected by x-ray diffraction (XRD) around the resistivity minimum, which is due to the small grain size of the zinc and the alumina phases. As can be seen from figure 14 not only the charge carrier concentration decreases with increasing oxygen partial pressure, but also the Hall mobility. This is due to the influence of the grain barriers on the electrical transport. Decreasing charge carrier concentrations increase the potential barrier between the grains leading to lower mobilities [41].

An interesting result is obtained when the electrical parameters, i.e. carrier concentration and mobility, are depicted as a function of grain size (derived from the XRD spectra, see section 4.2). Both quantities exhibit a strong dependence on the crystallographic perfection of the films, i.e. on the grain size (see figure 16). This is evidence for the decisive role of the crystalline quality (grain size, strain, defects) of the zinc oxide films on the electrical properties.

**Table 2.** Properties of the TCO materials.

Property	In <sub>2</sub> O <sub>3</sub>	SnO <sub>2</sub>	ZnO
Mineral name	—	cassiterite	zincite
Band gap $E_g$ (eV)	3.75	3.7	3.4
Melting point (°C)	≈2000	>1930*	1975
Heat of formation (eV)	9.7	6.0	3.6
Density (g cm <sup>-3</sup> )	7.12	6.99	5.67
Relative permittivity	9	9	8.1
Effective electron mass $m^*/m_e$	0.3	0.28	0.28
Dopants	Sn, Ti, Zr, F, Cl	Sb, (As, P), F, Cl	B, Al, In, Ga, Si, Sn, F, Cl
Crystal structure, space group	cubic I2 <sub>1</sub> 3	tetragonal, rutile $P4_2/mnm$	hexagonal, wurtzite $P6_3/mc$
Lattice parameters (nm)	$a$ : 1.012	$a$ : 0.474 $c$ : 0.319	$a$ : 0.325 $c$ : 0.5207
Thermal expansion $\alpha$ (300 K) (K <sup>-1</sup> )	6.7	$\parallel c$ : 3.7 $\perp c$ : 4.0	$\parallel c$ : 2.92 $\perp c$ : 4.75
Melting point of the metal (°C)	157	232	420
Average amount of the metal in the earth's crust (ppm)	0.1	40	132

\* Decomposition into SnO and O<sub>2</sub> at 1500 °C.**Figure 18.** Compilation of electrical data from the literature of the last 20 years of doped ZnO films deposited by (reactive) magnetron sputtering (see table 3). Details are explained in the text.

The importance of the ion assistance during the growth process was recently investigated by our group [16]. Using the method of combined rf and dc excitation of a magnetron discharge the energetic bombardment of the growing film can be varied continuously. The dependence of  $\rho$ ,  $N$  and  $\mu$  for ZnO:Al films prepared with different  $P_{dc}/(P_{dc} + P_{rf})$  ratios is shown in figure 17. It can be seen that the rf discharge leads to films of 2.5 times lower resistivity compared to dc excitation. This decrease is due to an increase of  $N$  and  $\mu$ . From the structural analysis of these films it was found that this increase is caused by the lower mechanical stress in rf sputtered films. The grain size of the films did not change when  $P_{dc}/(P_{dc} + P_{rf})$  was varied (see section 4.2). Although ion bombardment can be advantageous for low-resistivity TCO films one has to be careful concerning the energies of the bombarding species (see also section 3). Too high energies

(higher than about 50 eV [42]) of the species impinging on the growing film lead to crystallographic damage in the films, which cause higher resistivities and lower mobilities [33, 43]. Using low discharge voltages (rf excitation) or high working pressures this bombardment problem for film growth can be avoided. Results from the literature for magnetron-sputtered doped ZnO films are summarized in figure 18 and table 3. From this compilation the following conclusions can be drawn.

- The dopant for zinc oxide most often used is aluminium. However, other dopants (B, Ga, In, Si) lead to resistivities comparable to Al-doped films.
- The lowest resistivity for polycrystalline ZnO films is about  $2 \times 10^{-4} \Omega \text{ cm}$ , and a little bit lower for epitaxial ZnO films.

**Table 3.** Compilation of electrical parameters of zinc oxide films prepared by magnetron sputtering.

Material	Reference (year)	Target	$\rho$ ( $\Omega$ cm)	$N$ ( $\text{cm}^{-3}$ )	$\mu$ ( $\text{cm}^2 \text{ V s}^{-1}$ )	$T_{\text{sub}}$ ( $^{\circ}\text{C}$ )	$p$ (Pa)	Method <sup>a</sup>
ZnO:Al	Jäger <i>et al</i> [44] (1998)	Zn:Al	$4.2 \times 10^{-4}$	$2.6 \times 10^{20}$	57	300	0.21	DCRMS
		Zn:Al	$4.0 \times 10^{-4}$	$4.9 \times 10^{20}$	32	300	0.15	ACRMS
ZnO:Al	Menner <i>et al</i> [43] (1998)	ZnO:Al <sub>2</sub> O <sub>3</sub>	$7.7 \times 10^{-4}$	$4.2 \times 10^{20}$	19.5	RT	0.5	DCMS
ZnO:Ga	Menner <i>et al</i> [43] (1998)	ZnO:Ga <sub>2</sub> O <sub>3</sub>	$5.9 \times 10^{-4}$	$5.9 \times 10^{20}$	20	RT	0.5	DCMS
ZnO:Al	Cebulla <i>et al</i> [16] (1998)	ZnO:Al	$6.5 \times 10^{-4}$	$6.5 \times 10^{20}$	15	RT	0.8	RFMS
		ZnO:Al	$1.4 \times 10^{-3}$	$4.0 \times 10^{20}$	10	RT	0.8	DCMS
ZnO:Al	Kluth <i>et al</i> [45] (1998)	ZnAl <sub>2</sub> wt%	$2.7 \times 10^{-4}$	$8.4 \times 10^{20}$	28	270	0.5	DCRMS
ZnO:Al	Tominaga <i>et al</i> [46] (1998)	ZnO:Al <sub>2</sub> O <sub>3</sub> 2 wt%	$1.9 \times 10^{-4}$	$1.1 \times 10^{21}$	30	250	0.75	DCRMS
ZnO:Al	Park <i>et al</i> [47] (1997)	ZnO:Al <sub>2</sub> O <sub>3</sub>	$4.7 \times 10^{-4}$	$7.5 \times 10^{20}$	15	150	0.2	RFMS
ZnO:Al	Löffl <i>et al</i> [48] (1997)	ZnO:Al <sub>2</sub> O <sub>3</sub>	$2.8 \times 10^{-4}$	$5.8 \times 10^{20}$	39	270	0.38	RFMS
ZnO:Al	Ellmer <i>et al</i> [27] (1994)	Zn:Al 2 wt%	$4.5 \times 10^{-4}$	$8.0 \times 10^{20}$	17	RT	0.5	DCRMS
ZnO:Al	Nakada <i>et al</i> [49] (1994)	ZnO:Al <sub>2</sub> O <sub>3</sub> 2 wt%	$3.6 \times 10^{-4}$	$5.6 \times 10^{20}$	37	350	1.5	DCMS
ZnO:B		ZnO + B <sub>2</sub> H <sub>6</sub>	$4.0 \times 10^{-4}$	$2.6 \times 10^{20}$	60	200	1.5	DCMS
ZnO:Al + B		ZnO:AlB <sub>12</sub> 1 wt%	$6.5 \times 10^{-4}$	$2.4 \times 10^{20}$	40	200	1.5	DCMS
ZnO:Al	Schäffler and Schock [50] (1993)	ZnAl	$2.7 \times 10^{-4}$	$4.3 \times 10^{20}$	53	450	0.8	DCRMS
ZnO:Al	Konishi <i>et al</i> [51] (1992)	ZnO:Al 1.3 wt%	$5.3 \times 10^{-4}$	$5.6 \times 10^{20}$	20	200	0.1	DCRMS
ZnO:Al	Mauch and Schock [52] (1991)	ZnAl	$2.5 \times 10^{-4}$	$7.0 \times 10^{20}$	36	350	1.0	DCRMS
ZnO:Al	Harding <i>et al</i> [28] (1991)	ZnAl	$5.0 \times 10^{-4}$	—	—	180	0.2	DCRMS <sup>b</sup>
ZnO:In		ZnIn	$1.4 \times 10^{-3}$	—	—	220	0.2	DCRMS <sup>b</sup>
ZnO:Al	Igasaki and Saito [6] (1991)	ZnO:Al <sub>2</sub> O <sub>3</sub> 2 wt%	$1.4 \times 10^{-4}$	$1.3 \times 10^{21}$	34	150	1.33	RFMS <sup>c</sup>
ZnO:Ga	Choi <i>et al</i> [53] (1990)	ZnO:Ga <sub>2</sub> O <sub>3</sub> 5 wt%	$5.9 \times 10^{-4}$	$1.5 \times 10^{21}$	7	30	0.38	RFMS
ZnO:Al	Jin <i>et al</i> [37] (1988)	ZnO + Al 2 at%	$5.4 \times 10^{-4}$	$4.5 \times 10^{20}$	26	30	0.38	RFMS DCMS
ZnO:Al	Minami <i>et al</i> [54] (1989)	ZnO:Al <sub>2</sub> O <sub>3</sub> 2 wt%	$3.3 \times 10^{-4}$	$8.3 \times 10^{20}$	22.5	200	0.8	RFMS <sup>b</sup>
ZnO:Si		ZnO:SiO <sub>2</sub> 2 wt%	$3.9 \times 10^{-4}$	—	—	200	0.8	RFMS <sup>b</sup>
ZnO:In	Qiu <i>et al</i> [68] (1987)	ZnO:In <sub>2</sub> O <sub>3</sub> 2 wt%	$3.0 \times 10^{-4}$	—	—	30	0.38	RFMS <sup>b</sup>
ZnO:Al	Minami <i>et al</i> [55] (1985)	ZnO:Al <sub>2</sub> O <sub>3</sub> 2 wt%	$1.9 \times 10^{-4}$	$1.5 \times 10^{21}$	22	30	0.5	RFMS <sup>b</sup>
ZnO:B		ZnO:B <sub>2</sub> O <sub>3</sub> 4 wt%	$6.4 \times 10^{-4}$	$2.5 \times 10^{20}$	39	30	0.5	RFMS <sup>b</sup>
ZnO:Ga		ZnO:Ga <sub>2</sub> O <sub>3</sub> 2 wt%	$5.1 \times 10^{-4}$	$4.4 \times 10^{20}$	28	30	0.5	RFMS <sup>b</sup>
ZnO:In		ZnO:In <sub>2</sub> O <sub>3</sub> 2 wt%	$8.1 \times 10^{-4}$	$4.0 \times 10^{20}$	20	30	0.5	RFMS <sup>b</sup>
ZnO:O <sub>v</sub> <sup>d</sup>	Webb <i>et al</i> [56] (1981)	ZnO (Ar + H <sub>2</sub> )	$2.0 \times 10^{-3}$	$2.0 \times 10^{20}$	16	130	0.38	RFMS

<sup>a</sup> DCRMS is dc reactive magnetron sputtering, ACRMS is ac reactive magnetron sputtering, DCMS is dc magnetron sputtering, RFMS is rf magnetron sputtering.

<sup>b</sup> Substrate positioned perpendicular to the target.

<sup>c</sup> Epitaxial deposition onto (1-210)-oriented sapphire.

<sup>d</sup> O<sub>v</sub>, oxygen vacancies (intrinsic doping).

- The resistivity is inversely proportional to the carrier density (figure 18(c)) in agreement with the theory of ionized impurity scattering (see below).
- The Hall mobilities scatter between 10 and 60 cm<sup>2</sup> V s<sup>-1</sup> without a correlation to charge carrier concentration. These values are still lower than the mobility limit of 90 cm<sup>2</sup> V s<sup>-1</sup>, derived by Bellingham *et al* [57].
- While the Hall mobilities exhibit a tentative trend to increase with higher substrate temperatures (figure 18(b)),

the resistivities do not show any correlation with substrate temperature. Obviously, the other deposition conditions (plasma excitation, orientation of the substrate relative to the target) are also very important.

The lowest resistivity values for not intentionally heated substrates were reported for a special deposition method where the substrates are positioned not parallel but perpendicular to the target [33, 55]. These authors claim that this deposition configuration avoids the bombardment of the

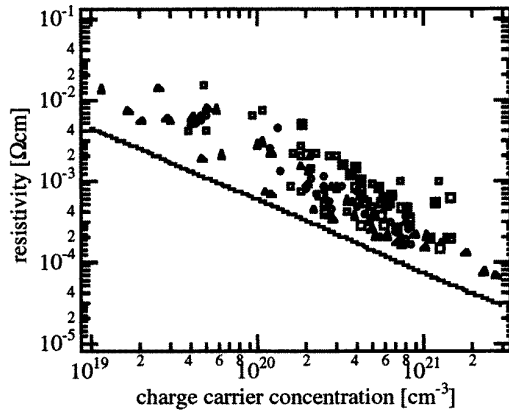


**Figure 19.** Resistivity of transparent conductive oxides depending on the charge carrier concentration. The open symbols are data from the literature for ITO ( $\Delta$ ), tin oxide ( $\circ$ ) and zinc oxide ( $\square$ ). Our own results for zinc oxide are displayed as full squares. The line is a theoretical lower limit of the resistivity calculated under the assumption of a limitation of the mobility by ionized impurity scattering [57].

films by high-energy particles such as negative oxygen ions and energetic argon neutrals, reflected at the target.

The fundamental physical limits of the resistivity of TCO films have been examined by Bellingham *et al* [57]. They compiled thin-film resistivity data for ITO, tin oxide and zinc oxide from the literature and compared it with a theoretical limit calculated for ionized impurity scattering. Figure 19 shows their compilation together with our own measurements which depend on the charge carrier concentration. All three oxides show a similar behaviour: the resistivity is inversely proportional to the charge carrier concentration and the theory of ionized impurity scattering sets a lower limit. At these high charge carrier concentrations the mobility is not limited by the potential barriers between the grains [41]. Among the three oxides ITO is approaching the theoretical limit at best, due to the fact that ITO films exhibit the highest mobilities reported for TCO films.

In 1955, Brooks [58] and Dingle [59] calculated the resistivity for an electron gas of density  $n$  that is scattered by ionized impurities [57]:

$$\rho = \frac{N_i Z^2 e^2 m^*}{24\pi^3 (\epsilon_0 \epsilon_r)^2 \hbar^3 n^2} f(k_F) \quad (6)$$

where  $N_i$  is the density of impurities with charge  $Ze$ ,  $\epsilon_r$  is the low-frequency relative permittivity and  $m^*$  is the effective mass of electrons in the conduction band. The slowly varying function  $f(k_F)$  is given by

$$f(k_F) = \ln(1 + \beta^2) - \beta^2/(1 + \beta^2) \quad (7)$$

and  $\beta = 2k_F/k_{TF}$ , where  $k_{TF}$  is the Thomas–Fermi screening wavevector. From (6) it is clear that oxygen vacancy doping (double charged, i.e.  $Z = 2$ ,  $N_i = n/2$ ) is not as effective as doping by metallic substitution (single charged, i.e.  $Z = 1$ ,  $N_i = n$ ):  $\rho$  (oxygen doping) =  $2\rho$  (metal doping). In other words, the mobility in metal-doped TCO films should be higher by a factor of two compared to oxygen vacancy doping. However, in the case of tin-doped indium oxide this was not observed [60]. What can be

stated is that the addition of the metallic dopants improves the temperature and oxidation stability of the TCO films. Taking these two facts into account there exists the possibility that the dopants (for instance Al, B, Ga, In and Si in zinc oxide) act as getters for oxygen through the formation of the corresponding oxide, thus creating oxygen vacancies in the TCO lattice.

From the relation  $\rho = (e\mu n)^{-1}$  and the approximated inverse proportionality of the resistivity on the carrier concentration (see figure 19) it follows that the limit of the ionized impurity scattering can be described by an electron mobility of about  $90 \text{ cm}^2 \text{ V s}^{-1}$ .

In summary it can be stated that the theoretical limit is nearly reached in the films prepared. The differences between the three types of oxides are not very large. The exact doping mechanism of the intrinsic (oxygen vacancies) and extrinsic dopants (for instance aluminium in ZnO or tin in ITO) is not clear at the moment [60].

A further increase of the charge carrier concentration is limited by a decrease of transmission in the infrared caused by free carrier absorption. Therefore, the only possibility to improve the electrical properties is to increase the mobility. This can be achieved by preparing films of better crystallographic properties (larger grains, lower mechanical stress). However, in homogeneously doped TCO films the mobility is also limited to values of about  $90 \text{ cm}^2 \text{ V s}^{-1}$  due to ionized impurity scattering. A promising way to improve the mobility in TCO films could be achieved by modulation doping, which has already been used, in the 1970s, to increase the mobility in  $\text{GaAs-Al}_x\text{Ga}_{1-x}\text{As}$  superlattices [61]. This concept uses multilayers of high- and low-doped semiconducting films. While the highly-doped layers deliver the charge carriers, the electron transport occurs preferentially in the low-doped layers whose mobility is not limited by ionized impurity scattering. The first attempts with the modulation doping concept for polycrystalline TCO films were reported by Rauf [62] and Tominga *et al* [46].

## 4.2. Structural and mechanical properties

It is well known from the literature that the structure of the ZnO films as revealed by XRD depends strongly on the preparation conditions. Zinc oxide exhibits a very pronounced (001) texture, that means, the  $c$ -axis of almost all (hexagonal) zincite crystallites is perpendicular to the substrate surface [63]. However, the extent of the texture, the grain size and the mechanical stress in the films depend significantly on the growth conditions, as shown for reactive magnetron sputtering in figure 20. Figure 20(a) displays the (002) diffraction peak for different oxygen partial pressures during rf sputtering. With rising oxygen partial pressure the peak intensity decreases, the width of the peaks broadens and the peak location is shifted to smaller values compared to the reference peak of zincite powder. These variations are due to:

- different grain sizes (broadening, low intensity) and
- internal compressive strain (peak shift).

Similar variations have been found for dc reactive magnetron sputtering. The grain size and the strain derived from the (002) peaks are shown in figure 20(b) depending on the

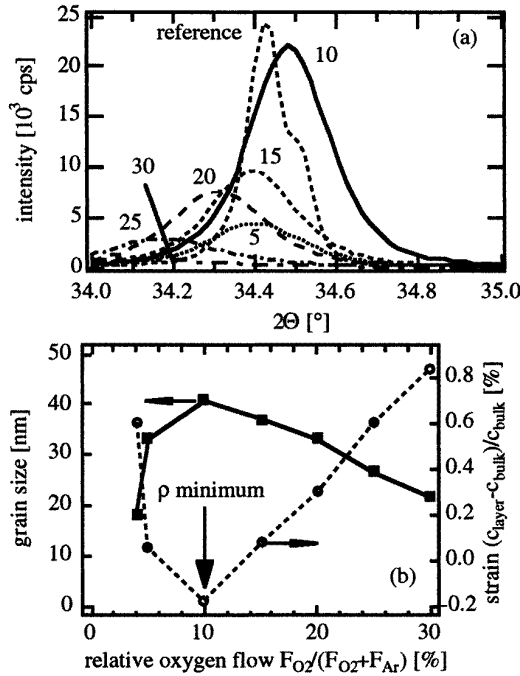


**Figure 20.** (a) (002) peak of ZnO:Al films reactively sputtered by rf excitation. The numbers at the peaks denote the relative oxygen flow. The reference peak was measured for a strain free zincite powder. (b) Grain size and strain of the layers from (a) against relative oxygen flow  $F_{O_2}/(F_{O_2} + F_{Ar})$  [63]. The vertical arrow marks the resistivity minimum which coincides with the strain minimum and the grain size maximum.

relative oxygen flow (and hence of the oxygen partial pressure). Interestingly, the layers with the lowest resistivities (marked by an arrow) exhibit the largest grains with the lowest strain. This is tentatively explained by the substitutional build-in of the dopant Al onto zinc lattice sites, thus leading to the most efficient doping of the films. At higher (and) lower oxygen concentrations in the sputtering atmosphere, alumina ( $Al_2O_3$ ) is formed, which segregates as a separate phase, thus introducing compressive strain in the films.

To further quantify the preferential orientation of the zinc oxide films pole figure measurements were performed. Typical pole figures of the (002) reflex of a low-resistant film (a) and a fully oxidized film (b) prepared by reactive rf sputtering from a Zn:Al 2 wt% target are shown in figure 21. The narrow peak around the tilt angle  $\chi = 0^\circ$  exhibits a rotational symmetry, which means that the crystallites have their  $c$ -axis perpendicular to the substrate with a mosaic spread around this axis. The fully oxidized film (figure 21(b)) displays, in addition to the narrow peak at  $\chi = 0^\circ$ , a lower intensity ring at  $\chi \approx 30^\circ$ , which points to the fact that the crystallites are less textured in these films. The intensity ring at about  $30^\circ$  in figure 21 is caused by crystallites of the (101) orientation, since the angle between the (001) and the (101) planes of zinc oxide is  $32^\circ$ . The development of a (101) texture of zinc oxide films was also observed by Minami *et al* [64] for Al-doped ZnO. These authors found that (101) textured ZnO films with a milky appearance could be prepared at high sputtering pressures, large thicknesses ( $> 1 \mu m$ ) and/or high substrate temperatures. In our experiments, the narrowest distributions

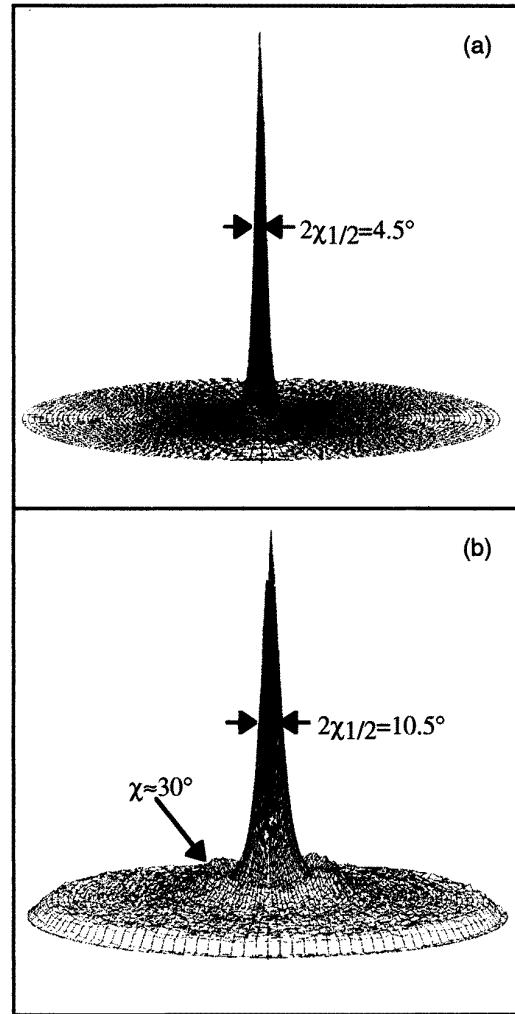


**Figure 21.** Texture distributions (pole figures) of the (002) line in three-dimensional representation (in polar coordinates) for two rf sputtered films, (a) sputtered at  $F_{O_2}/F_{total} = 10\%$  (resistance minimum) and (b) deposited at  $F_{O_2}/F_{total} = 30\%$  (isolating films). Sputtering parameters: ZnAl 2 wt% target,  $P_{rf} = 100$  W and  $P_{total} = 0.3$  Pa [63].

are observed for the layers with the lowest resistances. This is displayed in figure 22, where the  $\chi$  halfwidths as a measure of the texture are shown depending on the oxygen gas flow relative to the total gas flow together with the areas of the (002) peak. For an oxygen portion in the process gas of 10% (rf sputtering) the halfwidth is  $4.5^\circ$ . Increasing or decreasing the oxygen partial pressure leads to an increase of the halfwidth. This behaviour of the  $\chi_{1/2}$ -values is mirrored in the dependence of the (002)-peak areas. The most preferentially oriented films have the largest intensities of the (002) line, as expected.

In conclusion the texture, as quantified by pole figure measurements or from the (002) peak area depends on many deposition parameters, such as oxygen partial pressure, substrate temperature, ion assistance or from the dopant. This is compared for rf sputtered undoped and doped zinc oxide films in figure 23, which displays expanded XRD spectra of ZnO and ZnO:Al films of different thicknesses on a logarithmic scale [16]. At a larger thickness the zinc

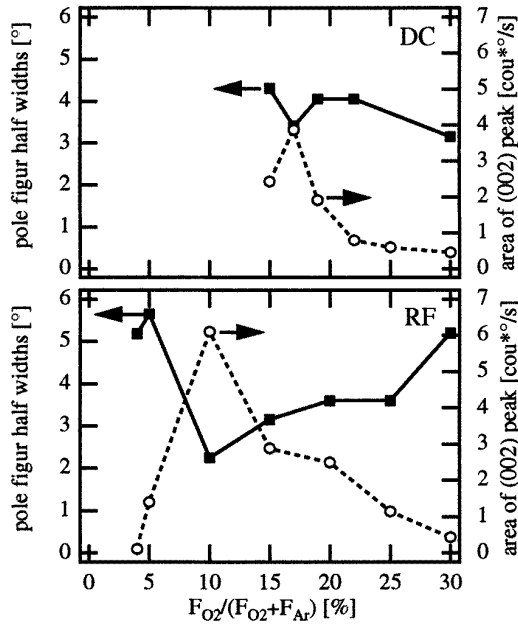


**Figure 22.** Half-widths (■) of the texture distributions and (002) peak area (○) in dependence on the oxygen flow (relative to the total flow) for dc and rf sputtered ZnO:Al films [63].

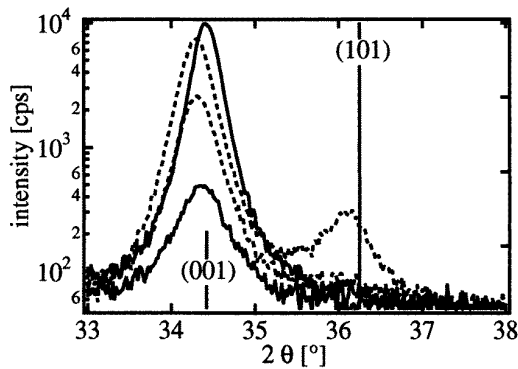


**Figure 23.** XRD spectra of rf sputtered ZnO (---) and ZnO:Al (—) films of different thicknesses. From bottom to top the films were 170 and 370 nm (ZnO) and 40 and 360 nm (ZnO:Al) thick. The vertical bars display the diffraction pattern of zincite powder (JCPDS data 36-1451) [16].

oxide films exhibit a (101) peak in addition to the dominating (002) peak. The aluminium-doped zinc oxide films do not show such a (101) peak, which is an indication of the better texture of the doped films. Such a behaviour was already found in the pole figures (figure 21), where the fully oxidized films had significant amounts of (101) oriented grains.

As a last example of the influence of the deposition conditions on structural properties of zinc oxide films the mechanical stress was measured for doped and undoped films. In micro-electronics and thin-film technology it is well known that mechanical stress influences not only the mechanical stability of thin film structures (adhesion) but also the electrical parameters. Ohler *et al* have shown that the lattice mismatch at a heterojunction significantly influences the band offsets. It is clear that different band offsets at a heterojunction lead to different electronic properties of a device made with this heterojunction. Former investigations

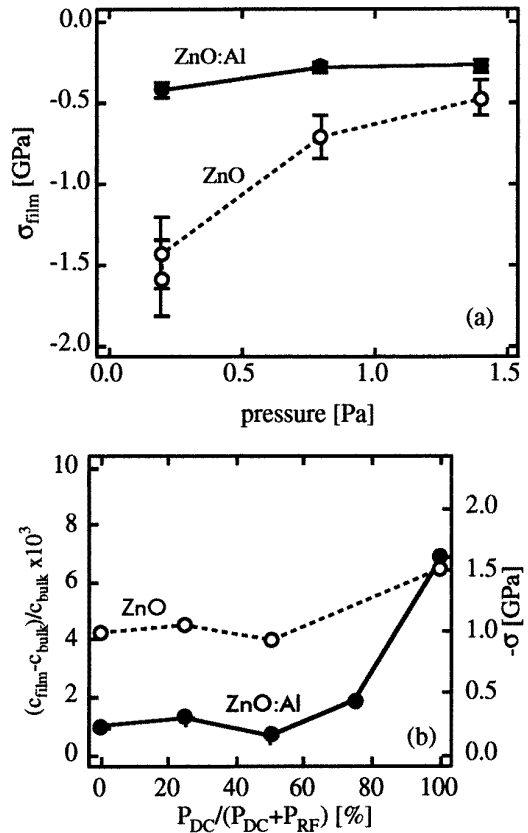


**Figure 24.** (a) Dependence of the film stress on the sputtering pressure for ZnO and ZnO:Al films with sputtering parameters:  $P_{rf} = 30$  W,  $d_{ZnO} = 120$  nm,  $d_{ZnO:Al} = 350$  nm [16]. (b) Strain (left) and stress (right) of ZnO and ZnO:Al films depending on the  $P_{dc}/(P_{dc} + P_{rf})$  ratio with sputtering parameters  $P_{dc} + P_{rf} = 80$  W and  $p_{Ar} = 0.8$  Pa [16].

in our group [66] of zinc oxide contact and window layers on CuInS<sub>2</sub> solar cells gave hints that excessive mechanical stress in the zinc oxide films decreases the efficiency of these cells.

In figure 24(a) the dependence of the stress on the sputtering pressure is displayed. The stress was determined *ex situ* by measuring the lattice constant (XRD) and by evaluating the bending of a thin cantilever coated with the films. All films exhibit compressive stress (negative stress values) which decreases in its absolute value by increasing the sputtering pressure. The undoped zinc oxide films show significantly larger stresses compared to the doped zinc oxide. In a difference to the behaviour of the sputtered metal films [67] no transition from compressive to tensile stress is observed for the zinc oxide films.

Figure 24(b) shows the dependence of the stress on the excitation conditions of the magnetron discharge (compare also with figure 17). Varying the ratio of dc-to-rf-power the stress can be influenced significantly. In a pure dc magnetron discharge the stress is higher than for depositions with at least 50% rf excitation. Again (see section 3.) the higher ion-to-neutral ratio for rf excitation improves the structural quality, in this case the stress state of the films. It is interesting to note that the grain size of the films does not change when varying the  $P_{dc}/(P_{dc} + P_{rf})$  ratio.

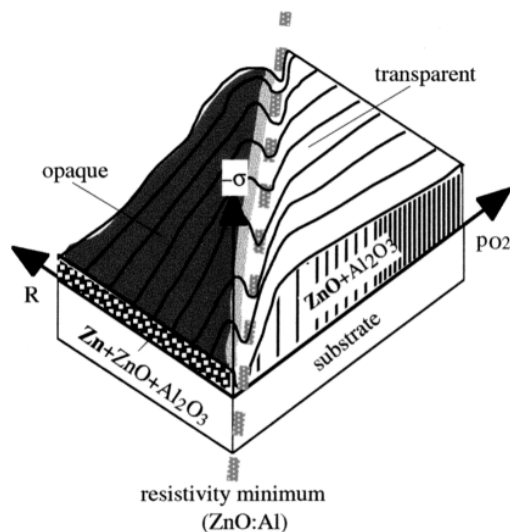


**Figure 25.** The structure–phase zone model for the reactive magnetron sputtering of zinc oxide films. The process parameters are the oxygen partial pressure  $p_{O_2}$  and the deposition rate  $R$  (discharge power). The vertical axis is the compressive stress ( $-\sigma$ ). The left dark triangular region corresponds to opaque films while the right ‘triangle’ represents the region of transparent films. The grain sizes and the phase composition are indicated in the two cross section areas. The technological process window falls into the ‘stress valley’ marked by the dashed line.

In summary the preparation of zinc oxide films, or more generally of TCO films, is a difficult balancing act of structure and phase composition of polycrystalline thin semiconducting films. Although the dopants are normally added in such amounts that sufficiently high charge carrier concentrations ( $>10^{21} \text{ cm}^{-3}$ ) could be achieved, only a part of the dopants are electrically active. Due to the interrelation between stoichiometry and structure, a fine tuning is necessary in order to prepare low-resistivity transparent films. From the results presented in sections 3 and 4 a structure–phase zone model in analogy to the well known structure zone model of Thornton [30] for magnetron sputtering of metals can be established that relates the phase composition (Zn, ZnO,  $\text{Al}_2\text{O}_3$ ), the mechanical stress, the transparency and the grain size with the deposition parameters of oxygen partial pressure and deposition rate (discharge power). Films of lowest resistivities are obtained in a relatively narrow process window (see figure 5), where large strain free crystallites exist, which consist mainly of the zinc oxide with the dopant on the zinc lattice sites. A deviation from this region in the structure–phase diagram (figure 25) changes the structure, the composition and the electrical and optical properties of the films. The best films can be prepared in the ‘stress valley’ extending from the lower left to the upper right. Similar diagrams can be constructed for the dependence of typical film properties on other preparation parameters such as sputtering pressure, substrate temperature, ion assistance during deposition etc.

## 5. Conclusions and outlook

For reactive and non-reactive magnetron sputtering of TCO films, especially of zinc oxide films, one has to achieve a

sensitive balance between the different deposition parameters (pressure, power/deposition rate, substrate temperature, energetic particle bombardment of the films) in order to get low-resistivity transparent films. Most investigations performed during the last two decades were restricted to the optimization of the deposition parameters.

Recently, a better physical understanding has been achieved concerning the relations between the plasma parameters (plasma density, discharge voltages, energies of energetic particles, energy input into the substrate etc.) and the TCO properties. Due to the three component system (metal, oxygen, dopant) and the polycrystalline nature of the thin films a fine tuning is necessary for good films. In a first attempt, a structure–phase zone model has been established for the preparation of Al-doped zinc oxide films by reactive magnetron sputtering.

An enhanced plasma density in front of the growing film is advantageous for preparing low resistivity TCO films at low substrate temperatures. However, it is important to restrict the energy of the bombarding species to values of about 50 eV. Higher energies lead to crystal damage and are detrimental for the film properties. Further work is needed to fully understand the relations between the extrinsic and intrinsic dopants, the grain and phase structure and the electrical transport properties of the TCO films.

A comparison of resistivity values of magnetron-sputtered ZnO films yields a limiting resistivity of about  $2 \times 10^{-4} \Omega \text{ cm}$  for polycrystalline films. Although a moderate improvement of the mobility values seems to be possible, an upper limit for  $\mu$  of about  $90 \text{ cm}^2 \text{ V s}^{-1}$  was estimated by Bellingham *et al* [57]. The following opportunities for future research can be deduced from this survey:

- construction of a more complete structure–phase zone model (such as shown in figure 25) for zinc oxide depending on the preparation parameters;
- thorough investigation of nucleation and film growth (especially by *in situ* techniques such as RHEED, XRD);
- better characterization of the discharge plasmas (Langmuir probes, optical emission spectroscopy, mass and energy spectroscopy of the species at the substrate, calorimetry);
- growth of epitaxial TCO films, in order to get a deeper insight into the role of crystallographic defects (point defects, twins, grain boundaries) for the electrical properties;
- microscopic investigations (for instance by EXAFS, XRD, EPR) of the role of intrinsic (oxygen vacancies) and extrinsic dopants on the electrical transport properties of zinc oxide;
- in order to overcome the ionized impurity scattering mobility limit of homogeneously doped TCO films, the modulation doping concept should be tested for polycrystalline TCO films.

## Acknowledgments

‘Fondest regards and many thanks to all the following characters’ (Eric Clapton) who contributed to the results: R Wendt, R Cebulla, R Mientus and F Kudella. H Tributsch is acknowledged for his continuous encouragement of this research.



## References

- [1] Schiller S, Heisig U and Goedicke K 1978 *Vakuum-Technik* **27** 51–5
- [2] Schiller S, Heisig U and Goedicke K 1978 *Vakuum-Technik* **27** 75–86
- [3] Kukla R, Krug T, Ludwig R and Wilmes K 1990 *Vacuum* **41** 1968–70
- [4] Szczyrkowski J, Dietrich A and Hartig K 1989 *Solar Energy Mater.* **19** 43–53
- [5] Kamei M, Shigesato Y, Yasui I, Taga N and Takagi S 1997 *J. Non-Cryst. Solids* **218** 267–72
- [6] Igasaki Y and Saito H 1991 *J. Appl. Phys.* **70** 3613–19
- [7] Penning F M 1936 *Physica* **3** 873–94
- [8] Thornton J A and Penfold A S 1978 *Thin Film Processes* ed J L Vossen and W Kern (New York: Academic) pp 75–113
- [9] Waits R K 1978 *J. Vac. Sci. Technol.* **15** 179–87
- [10] Thornton J A 1978 *J. Vac. Sci. Technol.* **15** 171–7
- [11] Yeom G Y and Kushner M J 1989 *J. Appl. Phys.* **65** 3816–24
- [12] Hofer W O 1990 *Scan. Microsc. Suppl.* **4** 265–310
- [13] Seah M P 1981 *Thin Solid Films* **81** 279–87
- [14] Yamamura Y and Itoh N 1989 *Ion Beam Assisted Film Growth* ed T Itoh (Amsterdam: Elsevier) pp 59–100
- [15] Nyairesh A R and Holland L 1981 *Vacuum* **31** 315–17
- [16] Cebulla R, Wendt R and Ellmer K 1998 *J. Appl. Phys.* **83** 1087–95
- [17] Wendt R, Ellmer K and Wiesemann K 1997 *J. Appl. Phys.* **82** 2115–22
- [18] Ellmer K, Wendt R, Diesner K and Fiechter S 1994 *Proc. 12th Eur. Photovoltaic Solar Energy Conf. (Amsterdam, April 11–15 1994)* (Bedford: H S Stephens) pp 1515–18
- [19] Okamoto A and Serikawa T 1986 *Thin Solid Films* **137** 143–51
- [20] Shinoki F and Itoh A 1975 *J. Appl. Phys.* **46** 3381–4
- [21] Aita C R 1985 *J. Vac. Sci. Technol. A* **3** 625–30
- [22] Schiller S, Heisig U, Steinfelder K, Strümpfel J, Voigt R, Fendler R and Teschner G 1982 *Thin Solid Films* **96** 235–40
- [23] Enjouji K, Murata K and Nishikawa S 1983 *Thin Solid Films* **108** 1–7
- [24] Szczyrkowski J, Teschner G and Bruch J 1997 *European patent specification* EP 0795623A1
- [25] Affinito J and Parsons R R 1984 *J. Vac. Sci. Technol. A* **2** 1275–84
- [26] Strümpfel J, Kammer M and Rehn S 1997 *Proc. 5. Tagung Neues Dresdner Vakuumtechn. Koll. (Dresden, October 16–17, 1997)*
- [27] Ellmer K, Kudella F, Mientus R, Schieck R and Fiechter S 1994 *Thin Solid Films* **247** 15–23
- [28] Harding G L, Window B and Horrigan E C 1991 *Solar Energy Mater.* **22** 69–91
- [29] Song P K, Shigesato Y, Yasui I, Ow-Yang C W and Paine D C 1998 *Japan. J. Appl. Phys.* **37** 1870–76
- [30] Thornton J A 1977 *Annual Review of Material Science* ed R A Huggins, R H Bube and R W Roberts (Palo Alto: Annual Review Incorporated) pp 239–60
- [31] Mattox D M 1989 *J. Vac. Sci. Technol. A* **7** 1105–14
- [32] Kersten H, Steffen H, Vender D and Wagner H E 1995 *Vacuum* **46** 305–08
- [33] Tominaga K, Kuroda K and Tada O 1988 *Japan. J. Appl. Phys.* **27** 1176–80
- [34] Petrov I, Hultman L, Sundgren J-E and Green J E 1992 *J. Vac. Sci. Technol. A* **10** 265–72
- [35] Gilmer G H and Roland C 1994 *Radiat. Eff. Def. Solids* **130/131** 321–43
- [36] Caporaletti O 1982 *Solar Energy Mater.* **7** 65–73
- [37] Jin Z-C, Hamberg I and Granqvist C G 1988 *J. Appl. Phys.* **64** 5117–31
- [38] Stjerna B and Granqvist C G 1990 *Thin Solid Films* **193/194** 704–11
- [39] Tominaga K, Ueda T, Ao T, Kataoka M and Mori I 1996 *Thin Solid Films* **281/282** 194–7
- [40] Wendt R and Ellmer K 1997 *Surf. Coatings Technol.* **93** 27–31
- [41] Tsurumi T, Nishizawa S, Ohashi N and Ohgaki T 1999 *Japan. J. Appl. Phys.* **38** 3682–8
- [42] Kubota E, Shigesato Y, Igarashi M, Haranou T and Suzuki K 1994 *Japan. J. Appl. Phys.* **33** 4997–5004
- [43] Menner R, Schäffler R, Sprecher B and Dimmler B 1998 *Proc. 2nd World Conf. Exhib. Photovoltaic Solar Energy Conf. (Vienna, July 6–10, 1998)* pp 660–3
- [44] Jäger S, Szyszka B, Szczyrkowski J and Bräuer G 1998 *Surf. Coat. Technol.* **98** 1304–14
- [45] Kluth O, Rech B, Houben L, Wieder S, Schöpe G, Beneking C, Wagner H, Löffl A and Schock H W 1998 *Proc. 2nd Int. Conf. Coat. Glass (Saarbrücken, Germany)*
- [46] Tominaga K, Umezue N, Mori I, Ushiro T, Moriga T and Nakabayashi I 1998 *Thin Solid Films* **334** 35–9
- [47] Park K C, Ma D Y and Kim K H 1997 *Thin Solid Films* **305** 201–9
- [48] Löffl A, Wieder S, Rech B, Kluth O, Beneking C and Wagner H 1997 *Proc. 14th Eur. Photovoltaic Solar Energy Conf. (Barcelona, June 30–July 4, 1997)* (Bedford: H S Stephens) pp 2089–92
- [49] Nakada T, Murakami N and Kunioka A 1994 *Proc. 12th European Photovoltaic Solar Energy Conf. (Amsterdam, April 11–15, 1994)* (Bedford: H S Stephens) pp 1507–10
- [50] Schäffler R and Schock H W 1993 *Proc. 23rd IEEE Photovoltaic Specialists Conf. (Louisville, KY, May 10–14, 1993)* pp 1026–30
- [51] Konishi R, Noda K, Harada H and Sasakura H 1992 *J. Cryst. Growth* **117** 939–42
- [52] Mauch R H and Schock H W 1991 *Proc. 10th Euro. Photovoltaic Solar Energy Conf. (Lisbon)* (Dordrecht: Kluwer) pp 88–91
- [53] Choi B H, Im H B, Song J S and Yoon K H 1990 *Thin Solid Films* **193/194** 712–20
- [54] Minami T, Sato H, Sonoda T, Nanto H and Takata S 1989 *Thin Solid Films* **171** 307–11
- [55] Minami T, Sato H, Nanto H and Takata S 1985 *Japan. J. Appl. Phys.* **24** L781–L784
- [56] Webb J B, Williams D F and Buchanan M 1981 *Appl. Phys. Lett.* **39** 640–2
- [57] Bellingham J R, Phillips W A and Adkins C J 1992 *J. Mater. Sci. Lett.* **11** 263–5
- [58] Brooks H 1955 *Adv. Electr. Electron Phys.* **7** 85
- [59] Dingle R B 1955 *Phil. Mag.* **46** 831–40
- [60] Bellingham J R, Phillips W A and Adkins C J 1991 *Thin Solid Films* **195** 23–31
- [61] Dingle R, Störmer H-L, Gossard A C and Wiegmann W 1978 *Appl. Phys. Lett.* **33** 665–7
- [62] Rauf I A 1993 *Mater. Lett.* **18** 123–7
- [63] Ellmer K, Diesner K, Wendt R and Fiechter S 1995 *Polycrystalline Semiconductors IV: Physics, Chemistry and Technology* ed S Pizzini, H P Strunk and J H Werner (Zug, Switzerland: Trans Tech) pp 541–6
- [64] Minami T, Sato H, Takata S, Ogawa N and Mouri T 1992 *Japan. J. Appl. Phys.* **31** L1106–9
- [65] Ohler C, Förster A, Moers J, Daniels C and Lüth H 1997 *J. Phys. D: Appl. Phys.* **30** 1436–41
- [66] Ellmer K, Cebulla R and Wendt R 1997 *Proc. MRS Spring Meeting (San Francisco, CA, March 31–April 4, 1997)* (Pittsburgh: MRS) pp 245–50
- [67] Hoffman D W and Thornton J A 1980 *J. Vac. Sci. Technol.* **17** 380–3
- [68] Qiu S N, Qiu C X and Shih I 1987 *Solar Energy Mater.* **15** 261–7